City Research Online

City, University of London Institutional Repository

1 # Aerodynamic breakup of an n-decane droplet in a high temperature

2 # gas environment

3

4 George Strotos[1,a,*], Ilias Malgarinos[1,b], Nikos Nikolopoulos[1,c], Manolis Gavaises[1,d]

5 [1]School of Engineering and Mathematical Sciences, City University London, Northampton

6 Square, EC1V 0HB, London, UK

7 [a] George.Strotos.1@city.ac.uk

8 [b] Ilias.Malgarinos.1@city.ac.uk

9 [c] Nikolaos.Nikolopoulos.1@city.ac.uk

10 [d] M.Gavaises@city.ac.uk

11 [*]Corresponding author

12

13 **Abstract**

14 The aerodynamic droplet breakup under the influence of heating and evaporation is studied

15 numerically by solving the Navier-Stokes, energy and transport of species conservation

16 equations; the VOF methodology is utilized in order to capture the liquid-air interphase. The

17 conditions examined refer to an n-decane droplet with Weber numbers in the range 15-90 and

18 gas phase temperatures in the range 600-1000K at atmospheric pressure. To assess the effect

19 of heating, the same cases are also examined under isothermal conditions and assuming

20 constant physical properties of the liquid and surrounding air. Under non-isothermal

21 conditions, the surface tension coefficient decreases due to the droplet heat-up and promotes

22 breakup. This is more evident for the cases of lower Weber number and higher gas phase

23 temperature. The present results are also compared against previously published ones for a

24 more volatile n-heptane droplet and reveal that fuels with a lower volatility are more prone to

25 breakup. A 0-D model accounting for the temporal variation of the heat/mass transfer

26 numbers is proposed, able to predict with sufficient accuracy the thermal behavior of the

27 deformed droplet.

28 **Keywords:** droplet breakup; VOF; heating; evaporation

29

1 Introduction

31 The efficiency of spray combustion systems is determined by the dispersion of the spray

32 droplets which increase the surface area and subsequently the rates of heat and mass transfer.

33 Following the primary jet breakup, the produced droplets are subjected to secondary breakup

34 which further enhances the heat/mass transfer rates. The coupled problem of secondary

35 droplet breakup under the influence of heating and evaporation is of major engineering

36 interest, but due to its complexity has not been yet addressed in detail and the vast majority of

37 relevant works examine these two phenomena independently.

38 Droplets under the influence of aerodynamic forces are subjected to different breakup modes,

39 namely the bag breakup, the transitional breakup, the sheet-thinning breakup and the

40 catastrophic breakup; for details see Guildenbecher et al. [1] among many others. The

41 outcome of the breakup is determined by the relative strength of the aerodynamic, surface

42 tension, viscous and external body forces acting on the droplet. These are grouped into

43 dimensionless numbers, forming the Weber number (We), the Reynolds number (Re), the

44 Ohnesorge number (Oh), the density ratio (ε) and the viscosity ratio (N), as shown in Eq. 1,

45 while under certain flow conditions other parameters such as the Froude number, the Mach

46 number and the turbulence levels may become important.

$$We = \frac{\rho_g U_{rel,0}^2 D_0}{\sigma} \quad Re = \frac{\rho_g U_{rel,0} D_0}{\mu_g} \quad Oh = \frac{\mu_l}{\sqrt{\rho_l \sigma D_0}} \quad \varepsilon = \frac{\rho_l}{\rho_g} \quad N = \frac{\mu_l}{\mu_g} \tag{1}$$

47

48 The phenomena observed during droplet breakup have been addressed in review studies such

49 as those of [1-5] among others; it is generally considered that the *We* number is the most

50 influential parameter, while viscous effects become important when *Oh*>0.1. The breakup

51 process requires some finite time to be established and the duration of the phenomenon is in

52 the order of the shear breakup timescale t_{sh} proposed by Nicholls and Ranger [6]:

$$t_{sh} = \frac{D_0}{U_{rel,0}} \sqrt{\varepsilon} \tag{2}$$

53

54 Many works have studied either experimentally or numerically the droplet breakup, aiming to

55 enlighten the conditions leading to the different breakup regimes and the underlying physics.

56 Selective experimental studies on droplet breakup are those of [7-22] but generally, there is a

57 scattering of the experimental findings which is probably due to the variety of the

58 experimental techniques used and the experimental uncertainties. Numerical works aiming to

59 fill the gap in knowledge such as those of [23-32]; they have examined the isothermal droplet

60 breakup in 2-D and 3-D computational domains and they have provided useful information

61 into the detailed processes inside and in the vicinity of the droplets during droplet breakup,

62 which are difficult to be determined with experimental techniques. More specifically, [7-10]

63 provided breakup maps in the *We-Oh* plane, [11-13, 16] further clarified the boundaries

64 between different breakup regimes, [14, 15, 20, 23, 25, 30, 31] clarified the physical

65 mechanisms behind the breakup regimes, [13, 18] examined the size distribution of the child

66 droplets after the parent droplet disintegration, [22] identified experimentally the gas flow

67 structure during droplet breakup, [15, 24, 26, 32] examined the effect of density ratio and [26,

68 27, 29, 31] examined the droplet drag coefficient. For a detailed presentation of the works

69 referring to droplet breakup, see Strotos et al. [33].

70 Regarding the evaporation studies, in addition to 0-D or 1-D models (see details in the review

71 articles of [34-37] among others), detailed CFD works solving the complete Navier-Stokes

72 and heat/mass transfer equations have also been published. Selectively, the works of [38-47]

73 refer to single component evaporation and [48-53] refer to multicomponent droplet

74 evaporation, providing detailed information in the transport processes between the liquid and

75 the gas phase. More specifically, [39, 40] were the first who solved the complete set of the

76 governing equations, [42, 47] modelled the presence of the suspender, [43] examined the

77 effect of thermocapillary flow, [44] studied the effect of turbulence and [46] proposed

78 numerical improvements for the evaporation modelling. Similarly, in multicomponent studies

79 the first ones were those of [48, 49], followed by [50] who included variable thermophysical

80 properties and [52, 53] which conducted parametric studies. The aforementioned studies were

81 restricted to the modelling of isolated spherical droplets and a detailed presentation of the

82 works referring to droplet evaporation, was given in Strotos et al. [54].

83 Regarding the coupled problem of droplet breakup and evaporation, this has not yet been

84 studied in detail except in the CFD works of [55-60]. Haywood et al. [55, 56] showed that for

85 droplets under steady or unsteady (oscillatory) deformation, the quasi-steady correlations for

86 Nusselt (Nu) and Sherwood (Sh) numbers are still valid when a volume-equivalent diameter is

87 used, Mao et al. [57] showed that the mass transfer from deformed droplets is mainly

88 controlled by the Peclet (Pe) number, while the We number has a small impact only at high

89 Pe numbers. Hase and Weigand [58] studied the effect of droplet deformation on the heat

90 transfer enhancement and they found that this increases due to the oscillatory droplet motion

91 and the increased surface area of the deformed droplets; moreover, the steady-state classical

92 correlations for the Nu number, under-predict the heat transfer at the beginning of the

93 simulation. Later, Schlottke et al. [59] included the evaporation in their model and they found

4

94   that the droplet heating is affected by the flow field inside the droplet which transfers hotter

95   fluid from the droplet surface towards inside. Cerqueira et al. [60] studied spherical and

96   deformed rising bubbles and proposed new correlations for the *Nu* and *Sh* numbers.

97   The aforementioned studies were restricted to *We* number below 10, which limits the results

98   to small droplet deformation without breakup. Recently, Strotos et al. [61] examined the

99   effect of heating and evaporation in cases undergoing breakup for *We*=15-90. They examined

100 volatile n-heptane droplets and they showed that the droplet heating becomes increasingly

101 influential during breakup for lower *We* number and higher gas temperature. The present

102 numerical work is a continuation of this work and examines an n-decane droplet with

103 substantially lower volatility than the n-heptane; this promotes the higher heating of the

104 droplet. This work is the first examining the combined effect of heating and breakup solving

105 the Navier-Stokes, energy and transport of species equations coupled with interface capturing,

106 for a wide range of We numbers, gas phase temperatures for this particular fuel while it

107 compares it with the less volatile one for similar flow conditions. The structure of the paper

108 includes a brief description of the numerical model and the cases examined, followed by the

109 results, while the most important conclusions are summarized at the end.

110

2   Numerical model and methodology

112 The continuous field representation of the two-phase flow with the VOF methodology is used

113 to study the droplet breakup. The problem is assumed to be 2-D axisymmetric and an

114 automatic local grid refinement technique [62, 63] enhances the accuracy of the computations

115 at the interface region, while achieving low computational cost compared to a simulation with

116 a uniform grid of the same density. The droplet heating and evaporation are accounted for by

117 solving the energy and vapor transport equations, while the local evaporation rate is obtained

118 by using a model based on Fick's law, which is independent of the droplet shape. The species

5

119 properties depend on the local temperature [64, 65] and mass averaging rules are used for the

120 gaseous mixture assuming incompressible ideal gas. For the complete presentation of the

121 equations solved, the reader is referred to Strotos et al. [54]. The simulations were performed

122 with the commercial CFD tool ANSYS FLUENT v14.5 [66] and the numerical settings

123 adopted as also the User Defined Functions (UDFs) are identical to those used in Strotos et al.

124 [61].

125 The model has been successfully validated in [33, 54, 63, 67, 68] for cases including the

126 motion of a free falling droplet, droplet breakup, droplet evaporation and droplet impact onto

127 a solid substrate.

128

3 Results and discussion

3.1 Cases examined and numerical setup

131 The cases examined are similar to those presented in Strotos et al. [61] for a volatile n-

132 heptane droplet (C07), but this time an n-decane (C10) droplet is examined which has a much

133 lower volatility (i.e. vapor pressure) than the n-heptane. The cases examined refer to a small

134 100μm diameter droplet with an initial temperature of T_0=300K, corresponding to Oh=0.02

135 which is low enough to guarantee breakup process almost independent from the Oh number.

136 The droplet is assumed to be initially motionless and it is subjected to a step change of the gas

137 phase velocity leading to We numbers in the range 15-90. The ambient air has a high

138 temperature in the range 600-1000K ($T_{cr,C10}$=617.7K) which correspond to high density and

139 viscosity ratios (ε>1200 and N>20 respectively) and thus the breakup outcome is not affected

140 by them since ε>32 [24]. The aforementioned combination of We numbers and gas phase

141 temperatures corresponds to gas phase velocities in the range 77-243m/s; these in turn

142 correspond to Re numbers in the range 84-367 which ensures that the flow remains laminar

6

143   and axisymmetric [69, 70]; the Mach numbers are below 0.38, which implies that the

144   compressibility effects can be ignored. For all cases examined, the ambient pressure is

145   atmospheric; thus no modifications capturing high pressure effects are required in the

146   evaporation model. A graphical representation of the cases examined is shown in Fig. 1 on the

147   *We-Re* map. These cases were examined both for evaporating and isothermal conditions. For

148   the latter, the energy equation and the evaporation source terms were not accounted for, while

149   the species properties were kept constant at their reference temperature values, i.e. at

150   T_0=300K for the liquid droplet and at T_∞ for the surrounding air; the isothermal runs

151   correspond to a parametric study for the effect of *We* and *Re* numbers.
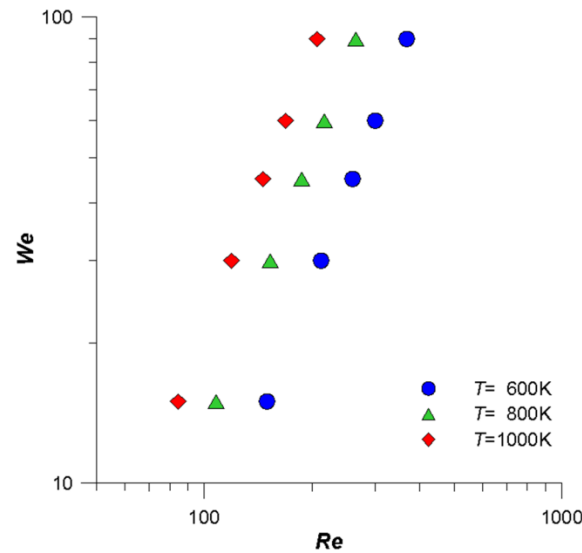
152

153

154   Fig. 1: Cases examined on the *We-Re* plane.

155

156   Regarding the computational domain and the boundary conditions, these are the same as in

157   Strotos et al. [33, 61, 68], in which a step change of the gas phase velocity is applied around

158   the initially motionless droplet; the 2-D axisymmetric computational domain is moving with

159   the average translational droplet velocity. Upwind the droplet, Dirichlet boundary conditions

7

160 were applied (i.e. fixed velocity and temperature for the non-isothermal cases) and downwind

161 Neumann boundary conditions (i.e. zero first gradient for all variables) were used. A locally

162 refined grid with 192 cells per radius was used, able to resolve the boundary layers at the

163 interface region as explained in Strotos et al. [61]. It has to be noted that the 2D simulations

164 performed in this work are considered reliable up to the breakup instant, since after that,

165 three-dimensional phenomena appear.

166 In an effort to relate and also distinguish the simulations performed in Strotos et al. [61] for

167 the volatile n-heptane droplet, from the present simulations referring to n-decane, the heat and

168 mass transfer Spalding numbers (B_T and B_M respectively) are considered (Eqs. 3 and 4). These

169 are calculated by using the initial surface temperature $T_{s,0}$ (Eq. 5) which corresponds to the

170 contact temperature between semi-infinite solids [71]; this concept was also used in [72-74]

171 for droplet impact on hot substrates and agrees well with the CFD predictions at the first time-

172 step.

$$B_{T,\infty} = \frac{c_{p,g,\infty}(T_\infty - T_0)}{L(T_{s,0})} \tag{3}$$

$$B_{M,0} = \frac{Y_s(T_{s,0}) - Y_\infty}{1 - Y_s(T_{s,0})} \tag{4}$$

$$T_{s,0} = \frac{\gamma_l T_0 + \gamma_g T_\infty}{\gamma_l + \gamma_g} \tag{5}$$

$$F_{heat} = \frac{1 + B_{T,\infty}}{1 + B_{M,0}} \tag{6}$$

173 The droplet's tendency to increase its temperature is proportional to B_T and inversely

174 proportional to B_M, since the evaporation absorbs heat and tends to decrease the droplet

175 temperature. An indicator of the droplet heat-up is the heating factor F_{heat} (Eq. 6); large values

176 imply a high tendency to increase the temperature. A comparison of the heating factor for the

177 n-heptane (C07) and the n-decane (C10) is shown in Fig. 2 as a function of the gas phase

8

178   temperature for T_0=300K (note that this is independent of the flow conditions). It is evident

179   that the n-decane has a higher possibility to heat-up due to its lower vapor pressure; the

180   heating factor increases with the gas phase temperature and decreases with increasing initial

181   fuel temperature (not shown in Fig. 2). It has to be noted that the heating factor has a

182   qualitative character and for the isothermal cases it was assumed that F_{heat}=1, which

183   corresponds to infinite latent heat and zero vapor pressure. Note that the definition of the

184   heating factor adopted here is suitable for the present conditions, but might not be suitable for

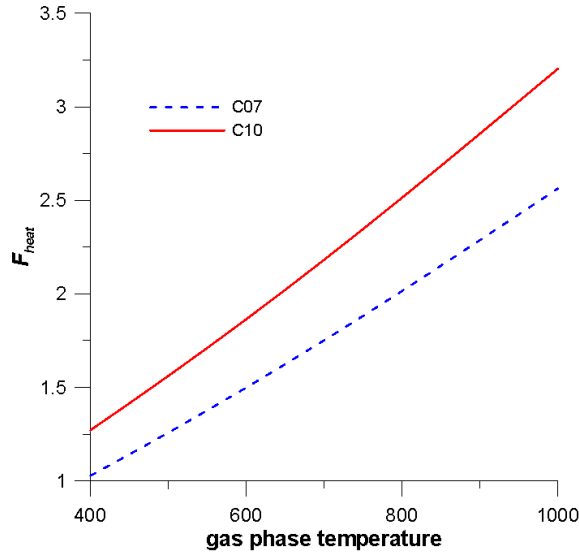185   low ambient temperatures close to the droplet temperature in which F_{heat}<1.

186

188   Fig. 2: Heating factor as a function of the gas phase temperature for two different fuels

189   (T_0=300K).

190

191   Finally, prior to the presentation of the results of the present work, it has to be noted that the

192   isothermal simulations conducted in Strotos et al. [61] for an n-heptane and the present

193   simulations for an n-decane are in close agreement between them since they both have low

194   Oh numbers (0.01 and 0.02 respectively) and similar Re number ranges (77-337 and 84-367

195   respectively for T_∞=600-1000K). On the other hand, the evaporating simulations for these two

196   fuels are exhibiting large variations due to the species thermal properties.

197

3.2 Hydrodynamic effect of heating

199   The results obtained for the droplet shapes are shown in Fig. 3 and Fig. 4 for the cases with

200   free stream temperature 800 and 1000K respectively. In these figures the left part corresponds

201   to the isothermal predictions and the right part to the evaporating simulations; the cases with

202   T_∞=600K are not presented since the differences between isothermal and evaporating

203   simulations were small. The droplet shapes drawn in black correspond to time intervals of

204   0.5t_{sh} (i.e. 0.0, 0.5, 1.0, 1.5, 2.0t_{sh}) and the droplet shapes drawn in red correspond to

205   intermediate instances i.e. 0.75, 1.25, 1.75, 2.25t_{sh} (the time instant of 0.25t_{sh} has been

206   omitted); the last droplet shape corresponds to the instant of breakup. From figures Fig. 3 and

207   Fig. 4 it is evident that the *We* number is the most influential parameter leading to different

208   breakup regimes as the *We* number increases, namely the bag breakup for low *We* numbers,

209   the transitional breakup for intermediate *We* numbers and the sheet-thinning breakup for the

210   highest *We* number examined. Nevertheless, the sheet-thinning breakup is not clear due to the

211   low *Re* number and the continuous transition between the different breakup regimes; the

212   effect of *Re* number and the existence of a critical *Re* number leading to bag breakup at

213   *We*=15 was in detail discussed in Strotos et al. [61] and similar comments were also made in

214   Han and Tryggvason [23] and Guildenbecher et al. [1].

215   Apart from the dominant role of *We* number, the droplet heating is playing an important role

216   for the low *We* number cases. Under isothermal conditions, droplets with *We*=15 and

217   T_∞>800K are not breaking up due to the low *Re* number. At the same *We* number when

218   heating is accounted for with T_∞=800K (Fig. 3), a clear bag breakup is predicted; this is even

219   more emphatic for the case of T_∞=1000K (Fig. 4) in which the droplet not only breaks up, but

the breakup regime predicted is the transitional breakup. To the authors best knowledge, no previous study has reported transitional break-up at such a low *We* number; this is purely due to the droplet heating which reduces the surface tension coefficient and subsequently the forces tending to resist the droplet deformation. Note that the effect of heating was not so profound in the high volatility n-heptane examined in Strotos et al. [61].
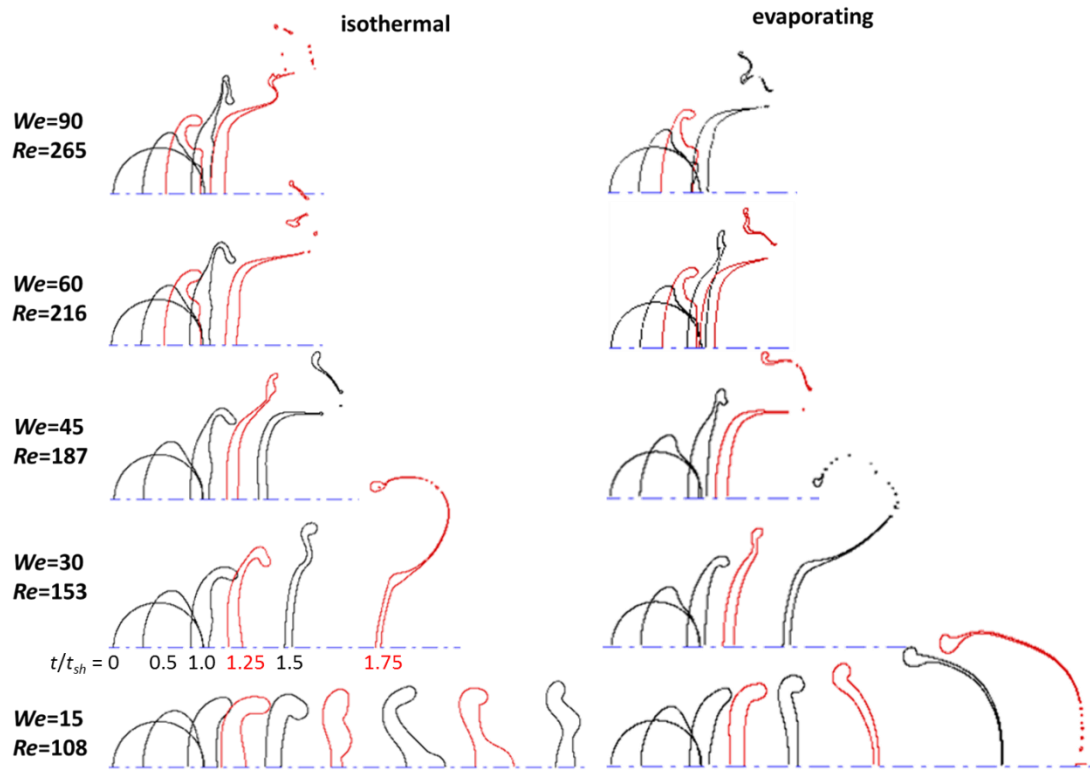

Fig. 3: Droplet shape evolution for the cases with T_∞=800K. The droplet shapes drawn black (see the online version) correspond to time intervals of $0.5t_{sh}$ and the droplet shapes drawn red correspond to representative intermediate instances of $0.25t_{sh}$. The last droplet shape corresponds to the instant of breakup. Differences are observed at the lower *We* number case.

11

Fig. 4: Droplet shapes for the cases with T_∞=1000K. The droplet shapes drawn black (see the online version) correspond to time intervals of $0.5t_{sh}$ and the drawn red correspond to representative intermediate instances of $0.25t_{sh}$. The last droplet shape corresponds to the instant of breakup. Differences are observed at the lower We number case.
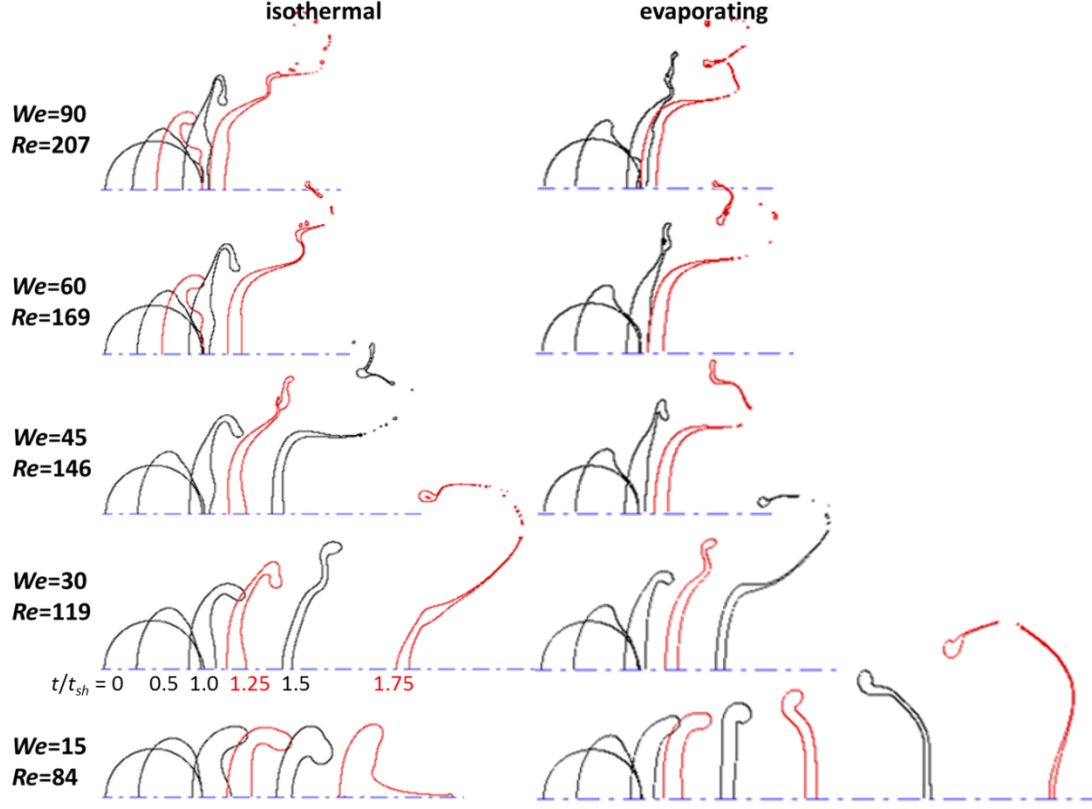
The predicted onset of breakup t_{br} (termed also as "initiation time") for all cases examined is shown in Fig. 5, along with the corresponding experimental correlations given by Pilch and Erdman [2] and Dai and Faeth [13], abbreviated as "P-E 1987" and "D-F 2001" respectively; the present data for the breakup time are subjected to error of the order of $0.05t_{sh}$ (2.5-5%) due to the estimation of the breakup time by examining post-processed images. The experimental correlations differ between them due to several experimental uncertainties [25]. The trends are correctly captured by predicting faster breakup with increasing We number. The isothermal cases exhibit a weak dependency on Re number when the We is kept constant,

12

246   while in the evaporating cases the reduction of the surface tension coefficient acts as if the *We*

247   number was higher; subsequently the droplet breaks up is faster. A best fit curve of the

248   breakup time for both evaporating and isothermal cases is given in Eq. 7 valid for the entire

249   range of conditions examined, i.e n-decane fuel, *Oh*=0.02, *We*=15-90, *Re*=84-367 and

250   T_∞=600-1000K.

$$t_{br}/t_{sh} = 8.628 We^{-0.352} Re^{-0.086} F_{heat}^{-0.116} \tag{7}$$
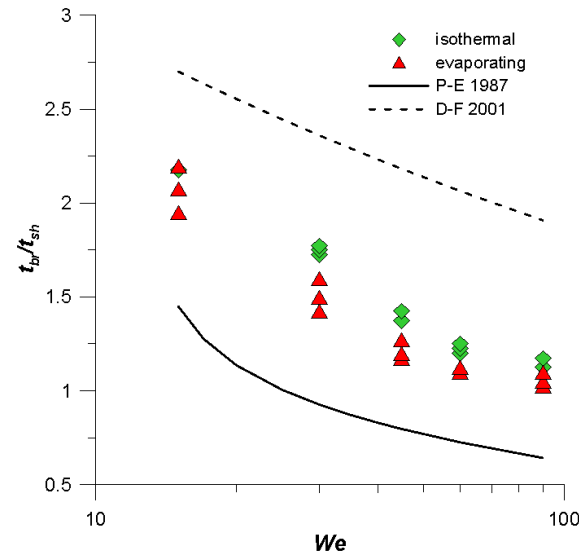
251

252

253   Fig. 5: Predicted dimensionless breakup time for the isothermal and the evaporating n-decane

254   cases.

255

256   One of the most important magnitudes determining the combustion efficiency is the droplet

257   surface area (*S*) which deviates significantly from the corresponding of the initial spherical

258   shape (*S₀*) during the droplet deformation and breakup and it is difficult to be measured

259   experimentally. The temporal evolution of this quantity is presented in Fig. 6 for selected

260   cases (*T*∞=800K and *We*=15, 30, 90); note that for the isothermal case with *We*=15, the

13

261   droplet is not breaking up. In all cases, after an initial non-deforming period of $\sim 0.3 t_{sh}$, the

262   droplet surface area starts to increase with a fast rate (1.6-5.7 in terms of non-dimensional

263   units) proportional to the *We* number, which is in accordance with the findings of Han and

264   Tryggvason [23]. Up to $t=t_{sh}$ the variation of the surface area is smooth, but at subsequent

265   times the rate of deformation may change due to surface instabilities appearing even in the

266   isothermal cases. For that reason, the maximum surface area at the instant of breakup is not

267   following a smooth variation as the *We* number is changing and a local maximum is observed

268   at *We*=30 (as it was also shown in [61]) reaching values of $12 S_0$. This point needs further

269   investigation by performing 3-D simulations since 3-D phenomena may appear before the

270   breakup instant and alter both the rate of deformation as also the breakup instant. Regarding

271   the effect of heating (see the solid lines in Fig. 6), it is evident that it is important for low to

272   medium *We* numbers and $t>t_{sh}$ by further increasing the rate of deformation.
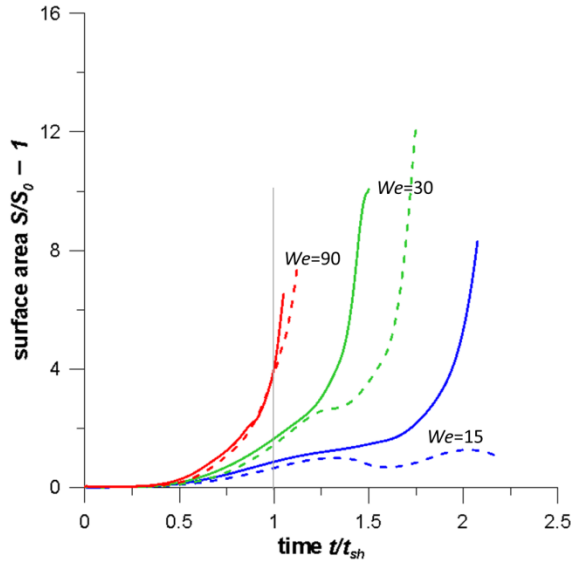
273

275   Fig. 6: Temporal evolution of the dimensionless droplet surface area for selected cases with

276   T_∞=800K. The dashed lines correspond to the isothermal cases and the solid lines to the

277   evaporating cases.

14

278

279   As explained in Strotos et al. [61] it is difficult to find a mathematical expression predicting

280   the temporal evolution of the surface area for the entire phenomenon up to the breakup instant

281   and covering the entire range of *We* numbers leading to different breakup regimes. This

282   becomes even more complex when heating is included since the surface area evolution is

283   implicitly coupled with the variation of the surface tension coefficient due to heating. On the

284   other hand, the evolution of the surface area can be predicted for $t<t_{sh}$ with Eq. 8a, which has

285   been slightly modified relative to the one used in [61] by using in the denominator on the

286   right hand side of Eq. 8a the term *sinh(c₂)*. Now, the coefficient c_1 expresses the surface area

287   at $t=t_{sh}$ and c_2 characterizes the form of the curve connecting the initial and the "final" state at

288    $t=0$ and $t=t_{sh}$ respectively; a low c_2 value implies a smoother (closer to the linear) variation.

289   An important improvement of the present fitting curve relative to the one in [61], is the

290   inclusion of the effect of heating by using the correction factor f_{corr} in the adjustable

291   coefficients c_1 and c_2 (see Eqs. 8b and c). Eq. 8 is valid for the entire range of conditions

292   examined in the present work, the correlation coefficient for the fitting of the surface area

293   evolution is above 0.98 and the prediction of the surface area at $t=t_{sh}$ is within the 15% error

294   for most of the cases examined; nevertheless this can reach values of 30% for specific cases at

295   the highest temperature of 1000K.

296

$$\frac{S}{S_0} - 1 = c_1 \frac{sinh(c_2 \cdot t/t_{sh})}{sinh(c_2)}, \qquad t < t_{sh} \tag{8a}$$

$$c_1 = 0.1484We^{1.092}Re^{-0.284}f_{corr}, \quad f_{corr} = 1 + 4.152We^{-1.06}(F_{heat} - 1)^{0.84} \tag{8b}$$

$$c_2 = 4.5234We^{0.294}Re^{-0.198}f_{corr}, \quad f_{corr} = 1 - 0.013We^{-0.50}(F_{heat} - 1)^{0.289} \tag{8c}$$

297

298   For the isothermal cases (f_{corr}=1) the surface area increases with increasing We number and

299   decreasing Re number; this is clearly derived from the sign of the exponents of c_1 (Eq. 8b).

300   When heating is included, the phenomenon becomes more complicated and the correction

301   factor f_{corr} depends both on the We number and the heating factor F_{heat}. The correction factor

302   for the coefficient c_1 is always f_{corr}>1 which means that heating tends to increase the surface

303   area at t=t_{sh}. As stated in [61], the extrapolation of this curve up to t_{br} should be done with

304   caution and limit the maximum value not to exceed 10-12S_0, otherwise unphysical values may

305   be obtained.

306   The droplet breakup is governed by the relative strength of the forces acting on the droplet,

307   which vary dynamically as the droplet shape, dimensions and velocity change during the

308   whole process. The instantaneous deforming forces scale with $\rho_g u_{rel,t}^2 D_{c,t}^2$ where $u_{rel,t}$ is the

309   instantaneous relative drop-gas velocity (obtained by subtracting the average droplet velocity

310   from the free-stream velocity) and $D_{c,t}$ is the instantaneous cross-stream diameter, while the

311   instantaneous restorative forces scale with $\sigma D_{c,t}$ in which the viscous forces have been ignored

312   since Oh<0.1. The ratio of these forces represents an instantaneous We number (see Eq. 9)

313   which changes during the breakup process and includes the effects of heating, deformation

314   and velocity change:

$$We_t = \frac{\rho_g u_{rel,t}^2 D_{c,t}}{\sigma} = We_0 \left(\frac{\sigma_0}{\sigma}\right)\left(\frac{D_{c,t}}{D_0}\right)\left(\frac{u_{rel,t}}{U_0}\right)^2 \qquad (9)$$

315   The predicted transient We number based on Eq. 9 is plotted in Fig. 7 for selected isothermal

316   and evaporating cases with T_∞=800K. The transient We number increases in time implying

317   that the deforming forces become progressively stronger, except of the isothermal case with

318   We=15. In this case the droplet is not breaking up and after reaching a maximum, the

319   instantaneous We number decreases, implying that the restorative forces become stronger.

320   Generally, the instantaneous We number (as defined in Eq. 9) increases by a factor of 2-3

321   relative to the initial We number which is mainly ought to the increase of the cross sectional

322 <mark>diameter; the reduction of the relative drop-gas velocity (no more than 10% for the cases</mark>

323 <mark>examined) and the reduction of the surface tension coefficient play a secondary role</mark>. In Fig. 7

324 the curves derived from Eq. 9 by using either the experimental breakup time of Dai and Faeth

325 [13] or that of Pilch and Erdman [2] for Oh=0.02 are also shown; these were derived by

326 processing the experimental data of [13] and more details can be found in [61]. These curves

327 represent the critical instantaneous condition for breakup and when crossed, breakup occurs.

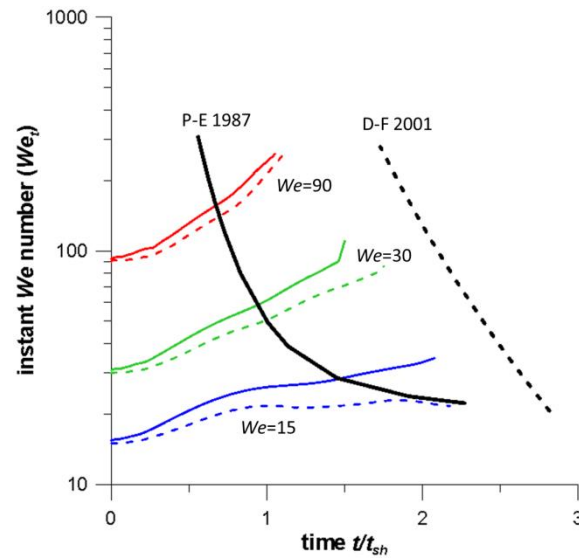328 The present simulations qualitatively agree with these curves.

329

330

331 Fig. 7: Predicted instant We number for selected isothermal (dashed lines) and evaporating

332 (solid lines) cases with T_∞=800K.

333

334 3.3 Thermal behavior of the droplet

335 The temporal evolution of the mean volume averaged droplet temperature T_m and the spatially

336 averaged surface temperature T_s are shown in Fig. 8a with the solid and dashed lines

337 respectively, for two cases combining different We numbers and gas phase temperatures;

17

338   these are indicated inside the parentheses as (We, T_∞). Both the mean droplet temperature and

339   the surface temperature increase with increasing ambient temperature, as expected. The mean

340   droplet temperature T_m increases continuously in time and may reach a heat-up of 15K by the

341   onset of breakup, while the average surface temperature T_s exhibits a quite transient behavior;

342   during the flattening phase ($t<0.6$-$0.8t_{sh}$) the surface temperature increases until reaching a

343   maximum, followed by a decrease until coming closer to the volume averaged temperature.

344   This behavior is mainly attributed to the flow patterns induced by the shape distortion which

345   exchange hotter fluid from the droplet surface with the colder fluid from the droplet interior

346   (see also Schlottke et al [59]). Additional to that, the increased surface temperature results in a

347   high evaporation rate which tends to further suppress the surface heating.

348   In Fig. 8b the dimensionless droplet mass and droplet volume (solid and dashed lines,

349   respectively) are shown for the cases (We, T_∞)=(15, 600) and (15, 1000). Up to the breakup

350   instant, the evaporated mass is less than 0.5%, while the droplet volume increases up to 0.1%

351   due to the thermal expansion effect. Note that in the corresponding cases with n-heptane

352   presented in [61], the maximum heat-up was 7K, the evaporated mass was reaching 2% and

353   the thermal expansion effect was absent. The aforementioned differences are mainly affected

354   by the different volatility between the n-heptane and n-decane.
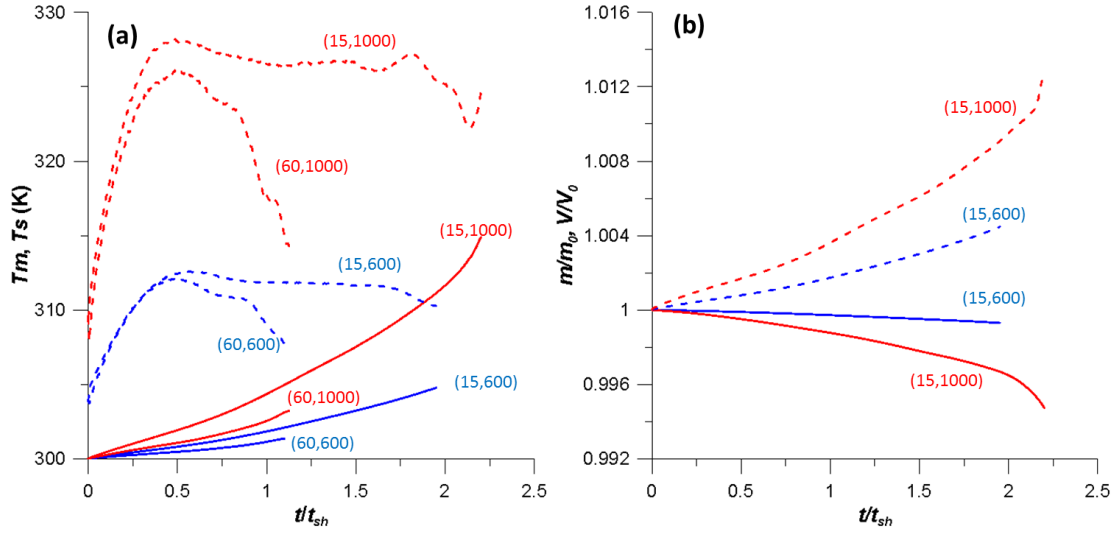
355

18

Fig. 8: (a) Temporal evolution of mean droplet temperature T_m (solid lines) and spatially averaged surface temperature T_s (dashed lines). In (b) temporal evolution of dimensionless droplet mass (solid lines) and dimensionless droplet volume (dashed lines). The cases shown in parentheses correspond to (We, T_∞).

The heat and mass transfer processes are usually characterized by the dimensionless Nusselt (Nu) and Sherwood (Sh) numbers respectively, which express the heat/mass transfer enhancement relative to a purely diffusive process. These are defined as the dimensionless temperature/concentration gradient at the droplet interface, but their calculation is not applicable with the VOF methodology due to the continuous variation of the field magnitudes across the interface as explained in [60]. Inspired by Hase and Weigand [58] an indirect method is used to estimate them, through the Eqs. 10-12:

$$\rho_l V \frac{d(c_{p,l}T_m)}{dt} = S\left(\frac{Nu \cdot k_{g,\infty}}{D_0}(T_\infty - T_s) - \dot{m}''L\right) \tag{10}$$

$$\dot{m} = S\frac{Sh \cdot \rho_{g,\infty}D_{AB,\infty}}{D_0}ln(1 + B_M) \tag{11}$$

19

$$Nu_l \cdot k_{l,0} \frac{T_s - T_m}{D_0} = Nu \cdot k_{g,\infty} \frac{T_\infty - T_s}{D_0} - \dot{m}''L \tag{12}$$

369

370   Eq. 10 is the droplet energy balance, Eq. 11 is a widely used relationship for the evaporation

371   rate of spherical droplets and Eq. 12 represents the heat flux continuity at the droplet's

372   surface, in which Nu_l is the dimensionless temperature gradient inside the liquid; this equation

373   connects the average droplet temperature T_m with the surface temperature T_s. The set of Eqs.

374   10-12 also forms a variant of the 0-D model for spherical droplet evaporation proposed by

375   Renksizbulut et al. [75]. Solving Eqs. 10-12 for Nu, Sh and Nu_{liq} and using the CFD data for

376   the mean droplet temperature T_m, the space averaged surface temperature T_s and the

377   evaporation rate dm/dt, the temporal variation of the dimensionless transfer numbers is

378   obtained; this is shown in Fig. 9 for the case $(We,T_\infty)=(15, 600)$, which can be regarded as

379   representative, since the qualitative behavior observed is similar in all cases examined. For

380   the Nu and Sh numbers, there is a short initial transitional period as the one observed in [39,

381   40, 58]; after that, they exhibit small fluctuations in time. The Sh number seems to oscillate

382   around a steady-state value, while the Nu number decreases continuously in time with a slow

383   rate. On the other hand, the Nu_{liq} number exhibits a more unsteady behavior. The initial

384   transitional period is longer compared to the other numbers and its magnitude exhibits almost

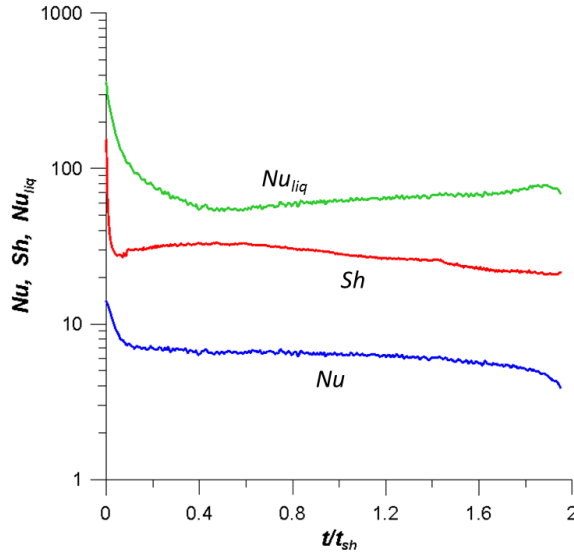385   one order of magnitude larger variations with time.

386

387

388   Fig. 9: Temporal variation of Nu, Sh and Nu_l for the case of $(We, T_\infty) = (15, 600)$.

389

390   It is of engineering interest to find expressions for the Nu, Sh and Nu_{liq} numbers and use them

391   in 0-D or 1-D models aiming to predict the droplet temperature and the evaporation rate.

392   Earlier CFD works on spherical droplets (see [39, 40] among many others) provided such

393   expressions as a function of the instantaneous Re, B_T and B_M numbers. Nevertheless, this is

394   not applicable in the case of droplet breakup due to the short duration of the phenomenon and

395   more importantly due to shape distortion from the spherical one. In [61] time-averaged

396   transfer numbers (being a function of the initial reference conditions) were used and they

397   could adequately capture the thermal behavior of droplets undergoing breakup. Following this

398   approach, the time-averaged transfer numbers fitting the present data are given in Eqs. 13-15;

399   the Re_l appearing in Eq. 15 ($Re_l = Re_\infty \varepsilon^{2/3} N^{-4/3}$) was taken from [38] and it is derived by

400   equating the tangential shear stresses at the droplet surface:

401

$$\overline{Nu} = \frac{2 + 6.83 Re_\infty^{0.07} Pr_{g,\infty}^{1/3}}{\left(1 + B_{T,\infty}\right)^{0.75}} \tag{13}$$

21

$$\overline{Sh} = \left(2 + 1.608 We_0^{0.591} Sc_{g,\infty}^{1/3}\right)\left(1 + B_{T,\infty}\right) \qquad (14)$$

$$\overline{Nu_l} = 55.95 + Re_l Pr_l^{1.6}/1429 \qquad (15)$$

402

403   The set of Eqs. 10-15 forms a 0-D model which can be used to predict the average droplet

404   heating and evaporation, but not the transient variation of the surface temperature, which

405   decreases after reaching a maximum (see Fig. 8a). The reason for that discrepancy is that the

406   time-averaged expressions ignore the transient behavior of the transfer numbers. In the

407   present work, the Nu and Nu_{liq} numbers are expressed as a function of the non-dimensional

408   time and this is an improvement of the model used in [61]; the correlations used are shown in

409   Table 1 and they are valid for the conditions examined in the present work.

410

411   Table 1: Transient Nu and Nu_{liq} numbers. The time t corresponds to the dimensionless time

412   t/t_{sh}.

	$Nu = c_0 - c_1 t + c_2 \exp(-c_3 t)$	$Nu_l = c_0 + c_1 \exp(-c_2 t) + c_3 \cos(2\pi t/c_4)$
c_0	$1.326 Re_\infty^{0.3647}\left(1 + B_{T,\infty}\right)^{-0.236}$	$56.47 + 7.65 \cdot 10^{-4} Re_l^{1.707}\left(1 + B_{T,\infty}\right)^{-0.432}$
c_1	$3 \cdot 10^{-6} Re_\infty^{2.212}\left(1 + B_{T,\infty}\right)^{2.226}$	$201 + 1.99 \cdot 10^{-4} Re_l^{2.25}\left(1 + B_{T,\infty}\right)^{-0.5285}$
c_2	3	$15.59 + 1.65 \cdot 10^{-6} Re_l^{2.64}\left(1 + B_{T,\infty}\right)^{-0.623}$
c_3	60	$5.786 \cdot 10^{-5} Re_l^{2.226}\left(1 + B_{T,\infty}\right)^{-0.825}$
c_4	–	1.2

413

414   The results of the 0-D model by using the transient correlations for Nu and Nu_{liq} are shown in

415   Fig. 10 for the case of $We=45$ and three different gas phase temperatures; the solid and the

416   dashed lines correspond to the CFD and the 0-D model predictions, respectively. As seen, the

417   time dependent expressions for the transfer number can adequately predict the transient

418   behavior of the surface temperature, with a less than 4K error. The model predictions

419   presented in Fig. 10 have assumed that the temporal evolution of the surface area is known

420   and this is a limitation of the proposed model. On the other hand, the Eq. 8 for the surface

421   area evolution can be used to predict the thermal behavior for $t<t_{sh}$; in this case, the errors are

422   mainly determined by the effectiveness of the curve reproducing the surface area evolution.
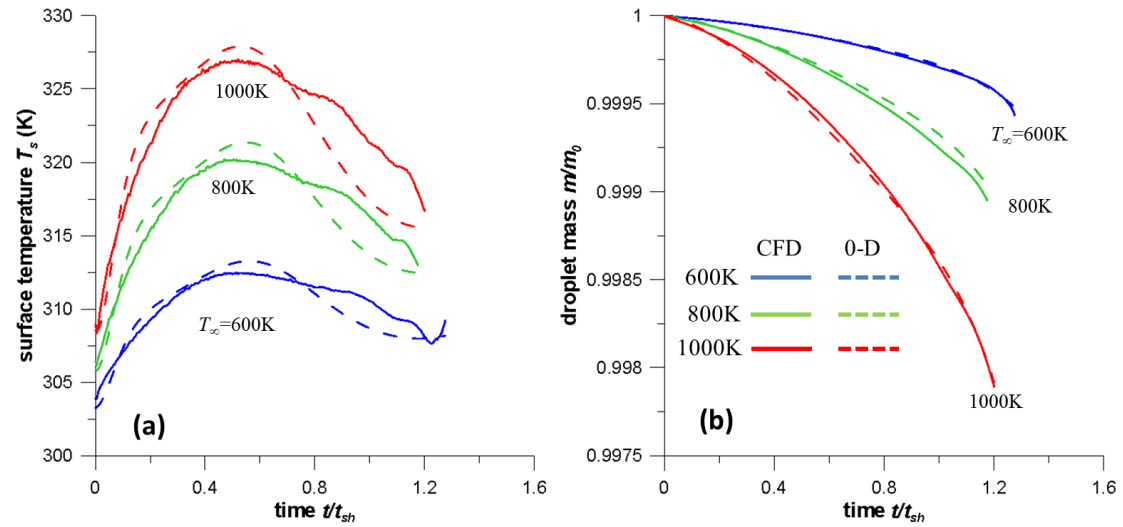
423

424

425   Fig. 10: Predictions of the 0-D model for (a) the spatially averaged surface temperature and

426   (b) the droplet mass for the case of $We=45$. The solid lines are the CFD data and the dashed

427   lines are the 0-D model predictions.

428

429   In Strotos et al. [61] it was shown that droplet breakup is affected by heating when the We

430   number is low and the ambient temperature is high. This conclusion was drawn both by

431 considering the associated timescales (either in a macroscopic or a microscopic level) and by

432 implementing the aforementioned 0-D model with the time-averaged expressions for the

433 transfer numbers. These comments are also verified by the present simulations for an n-

434 decane droplet. Relating the n-heptane CFD simulations performed in [61] and the present

435 ones for the n-decane, the surface temperature at $t=t_{sh}$ is well represented by Eq. 16. This

436 equation clearly demonstrates the effect of We number, gas phase temperature and species

437 volatility through the heating factor F_{heat}:

438

$$T_s(t_{sh}) = T_0\left(1 + 0.0195 We^{-0.2532} F_{heat}^{2.053}\right) \tag{16}$$

439

3.4 Spatial distribution of the flow variables

441 The spatial distribution of surface temperature, inner droplet temperature and vapor

442 concentration field are shown in Fig. 11 and Fig. 12 for the cases with $T_\infty=800K$ and We

443 number 15 and 30, respectively. The surface temperature (denoted with a thick line colored

444 with the corresponding temperature values) is not spatially uniform; along the droplet surface

445 differences of 15K can be observed. In the initial flattening phase, hot spots are observed on

446 the front side of the droplet in an off-axis location; at subsequent instances hot spots are

447 observed at the rear of the droplet. In a spherical droplet case these temperature differences

448 along the surface could induce secondary flow (due to surface tension gradients) and form

449 cellular vortices. The present work has included the effect of surface tension variation along

450 the interface through the CSS surface tension model [76]. Nevertheless, no secondary flow

451 was observed in the present cases (see characteristic streamlines in the left column), since the

452 flow patterns are determined by the droplet shape. Regarding the inner temperature field and

24

453 the vapor concentration field in the gas phase, these follow similar patterns to the ones

454 observed in [61], as affected by the local velocity field and the droplet deformation.
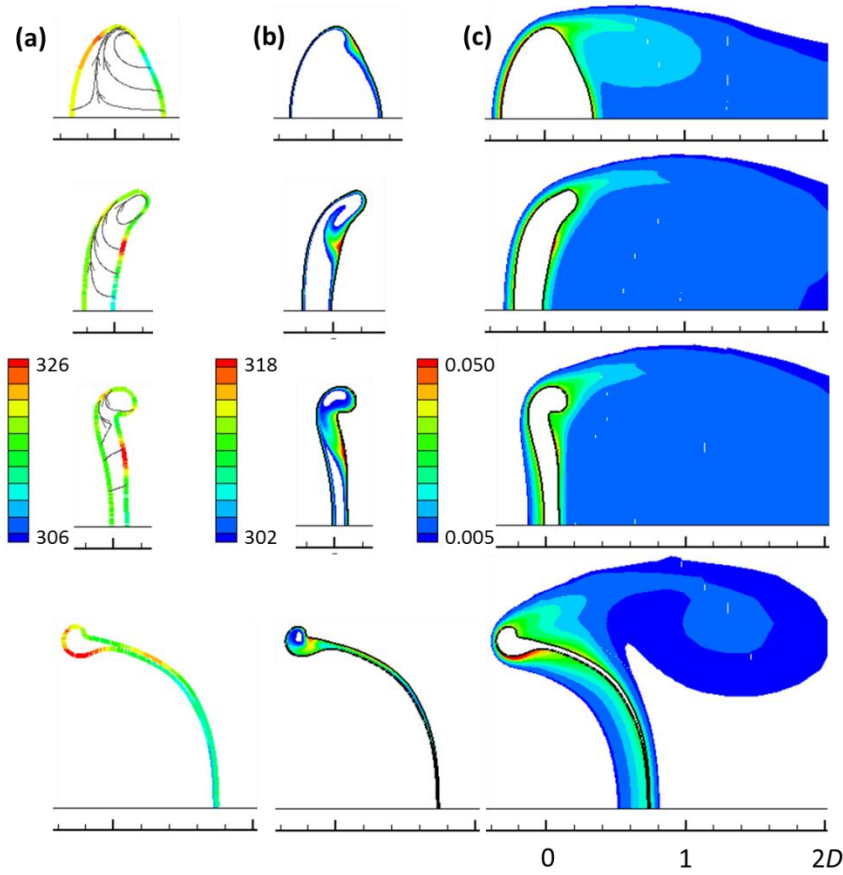
455

456

457 Fig. 11: Spatial distribution of (a) surface temperature, (b) droplet temperature and (c) vapor

458 concentration for the case (We, T_∞)= (15, 800). The time instances presented are 0.5, 1.0, 1.5

459 and $2.0t_{sh}$. In (a) characteristic streamlines are also shown. For color interpretation, see the
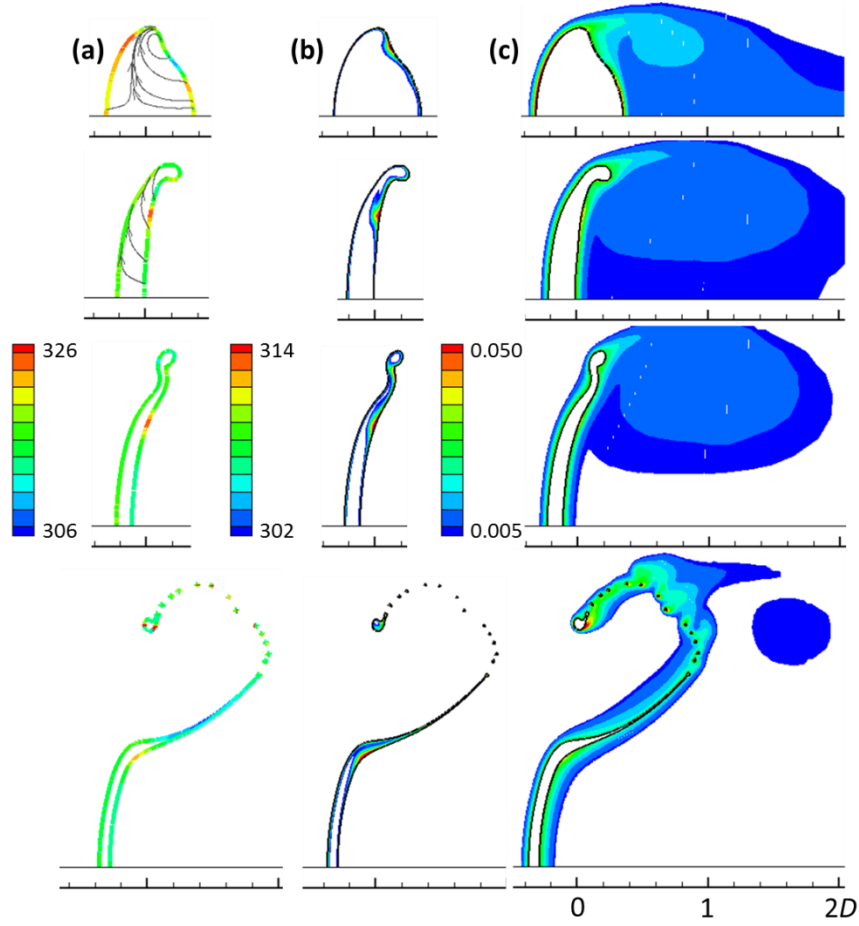
460 online version.

461

462

Fig. 12: Spatial distribution of (a) surface temperature, (b) droplet temperature and (c) vapor concentration for the case (We, T_∞)= (30, 800). The time instances presented are 0.5, 1.0, 1.25 and 1.5t_{sh}. In (a) characteristic streamlines are also shown. For color interpretation, see the online version.

467

4   Conclusions

The Navier-Stokes, energy and transport of species conservation equations together with the VOF methodology have been utilized to study the coupled problem of aerodynamic droplet breakup under the influence of heating and evaporation for We numbers in the range 15-90 and gas phase temperatures 600-1000K. To quantify the effect of heating, the same cases

26

473   were also studied under isothermal conditions assuming constant species properties.

474   Combining the results obtained from the present work for an n-decane fuel droplet with those

475   for a more volatile n-heptane droplet presented in Strotos et al. [61], it seems that droplet

476   heating affects the overall breakup performance for low We numbers, high gas phase

477   temperatures and low volatility fuels. For a non-breaking-up case with constant properties,

478   heating may decrease the surface tension coefficient in such a way, that droplet not only

479   breaks up in the bag breakup regime, but also in the transitional breakup regime.

480   Nevertheless, at high We numbers the surface tension still decreases but without altering the

481   breakup performance. During droplet breakup, despite the fact that the liquid evaporated mass

482   is very low (especially for low volatility fuels), one has to consider the evaporation source

483   terms since they play an important role by suppressing the droplet heat-up; this is evident for

484   high volatility fuels which seem to be less affected by heating.

485   The concept of "heating factor" was introduced which provides an indication of the droplet

486   tendency to heat-up by combining the terms tending to increase and decrease the droplet

487   temperature. Useful correlations were provided for an a-priori estimation of the breakup

488   instant, surface area evolution and droplet heat-up. Additional to them, an enhanced 0-D

489   model able to predict the thermal behavior of the droplet is proposed. In relevance to our

490   previous work [61], it uses time-dependent transfer numbers instead of time-averaged and it is

491   able to capture the transient behavior of the spatially average surface temperature. The latter

492   is not spatially uniform and peak values are observed in the front of the droplet in the initial

493   flattening phase and at the rear of the droplet in the subsequent stages.

494

5 Acknowledgements

6 Nomenclature

Roman symbols

Symbol	Description	Units
B_M	Mass transfer Spalding number	-
B_T	Heat transfer Spalding number	-
c_p	Heat capacity	J/kgK
D	diameter	m
D_{AB}	Vapor diffusion coefficient	m^2/s
F_{heat}	heating factor	-
Oh	Ohnesorge number $Oh = \mu_l/\sqrt{\rho_l \sigma D_0}$	-
k	Thermal conductivity	W/mK
L	Latent heat of vaporization	J/kg
m	mass	kg
$\dot{m}''$	Evaporation rate per unit area	kg/m^2s
Nu	Nusselt number	-
Pr	Prandtl number	-
R	radius	m
Re	Reynolds number $Re = \rho_g U_{rel,0} D_0/\mu_g$	-
S	surface area	m^2
Sc	Schmidt number	-
Sh	Sherwood number	-
t	time	s
t_{sh}	Shear breakup timescale $t_{sh} = D\sqrt{\varepsilon}/U$	-
T	temperature	K
U	reference velocity	m/s
u	instantaneous droplet velocity	m/s
V	volume	m^3
We	Weber number $We = \rho_g U_{rel,0}^2 D_0/\sigma$	-
We_t	instantaneous We number	-
Y	vapor concentration	kg/kg

Greek symbols

Symbol	Description	Units
a	thermal diffusivity	m^2/s
γ	thermal effusivity $\gamma = \sqrt{k\rho c_p}$	J/m^2K$s^{0.5}$

28

ε	density ratio $\varepsilon = \rho_l/\rho_g$	-
μ	viscosity	kg/ms
N	viscosity ratio $N = \mu_l/\mu_g$	-
v	kinematic viscosity	m^2/s
ρ	density	kg/m^3
σ	surface tension coefficient	N/m

505

Subscripts

Symbol	Description
0	initial
c	cross-stream
cr	critical
g	gas
l	liquid
rel	relative
s	at surface
t	instantaneous magnitude
x,y,z	coordinates
∞	free-stream conditions

506

Abbreviations

Symbol	Description
C07	n-heptane C_7H_{16}
C10	n-decane $C_{10}H_{22}$
CFD	Computational Fluid Dynamics
cpR	Cells per Radius
CSS	Continuum Surface Stress
UDF	User Defined Function
VOF	Volume of Fluid

507

References

509

510 [1] D.R. Guildenbecher, C. López-Rivera, P.E. Sojka, Secondary atomization, Experiments in
511 Fluids, 46 (2009) 371-402.

512 [2] M. Pilch, C. Erdman, Use of breakup time data and velocity history data to predict the
513 maximum size of stable fragments for acceleration-induced breakup of a liquid drop,
514 International Journal of Multiphase Flow, 13 (1987) 741-757.

515 [3] G.M. Faeth, L.P. Hsiang, P.K. Wu, Structure and breakup properties of sprays,
516 International Journal of Multiphase Flow, 21, Supplement (1995) 99-127.

29

[4] B.E. Gelfand, Droplet breakup phenomena in flows with velocity lag, Progress in Energy and Combustion Science, 22 (1996) 201-265.

[5] T.G. Theofanous, Aerobreakup of Newtonian and Viscoelastic Liquids, Annual Review of Fluid Mechanics, 43 (2011) 661-690.

[6] J.A. Nicholls, A.A. Ranger, Aerodynamic shattering of liquid drops, AIAA Journal, 7 (1969) 285-290.

[7] S.A. Krzeczkowski, Measurement of liquid droplet disintegration mechanisms, International Journal of Multiphase Flow, 6 (1980) 227-239.

[8] L.P. Hsiang, G.M. Faeth, Near-limit drop deformation and secondary breakup, International Journal of Multiphase Flow, 18 (1992) 635-652.

[9] L.P. Hsiang, G.M. Faeth, Drop properties after secondary breakup, International Journal of Multiphase Flow, 19 (1993) 721-735.

[10] L.P. Hsiang, G.M. Faeth, Drop deformation and breakup due to shock wave and steady disturbances, International Journal of Multiphase Flow, 21 (1995) 545-560.

[11] W.H. Chou, L.P. Hsiang, G.M. Faeth, Temporal properties of drop breakup in the shear breakup regime, International Journal of Multiphase Flow, 23 (1997) 651-669.

[12] W.H. Chou, G.M. Faeth, Temporal properties of secondary drop breakup in the bag breakup regime, International Journal of Multiphase Flow, 24 (1998) 889-912.

[13] Z. Dai, G.M. Faeth, Temporal properties of secondary drop breakup in the multimode breakup regime, International Journal of Multiphase Flow, 27 (2001) 217-236.

[14] Z. Liu, R.D. Reitz, An analysis of the distortion and breakup mechanisms of high speed liquid drops, International Journal of Multiphase Flow, 23 (1997) 631-650.

[15] C.H. Lee, R.D. Reitz, An experimental study of the effect of gas density on the distortion and breakup mechanism of drops in high speed gas stream, International Journal of Multiphase Flow, 26 (2000) 229-244.

[16] X.-K. Cao, Z.-G. Sun, W.-F. Li, H.-F. Liu, Z.-H. Yu, A new breakup regime of liquid drops identified in a continuous and uniform air jet flow, Physics of Fluids, 19 (2007) 057103.

545 [17] H. Zhao, H.-F. Liu, W.-F. Li, J.-L. Xu, Morphological classification of low viscosity
546 drop bag breakup in a continuous air jet stream, Physics of Fluids, 22 (2010) 114103.

547 [18] H. Zhao, H.-F. Liu, J.-L. Xu, W.-F. Li, K.-F. Lin, Temporal properties of secondary drop
548 breakup in the bag-stamen breakup regime, Physics of Fluids, 25 (2013) 054102.

549 [19] L. Opfer, I.V. Roisman, C. Tropea, Aerodynamic Fragmentation of Drops: Dynamics of
550 the Liquid Bag, in: ICLASS 2012, Heidelberg, Germany, 2012.

551 [20] L. Opfer, I.V. Roisman, J. Venzmer, M. Klostermann, C. Tropea, Droplet-air collision
552 dynamics: Evolution of the film thickness, Physical Review E, 89 (2014) 013023.

553 [21] D.R. Guildenbecher, P.E. Sojka, Experimental investigation of aerodynamic
554 fragmentation of liquid drops modified by electrostatic surface charge, Atomization and
555 Sprays, 21 (2011) 139-147.

556 [22] A.K. Flock, D.R. Guildenbecher, J. Chen, P.E. Sojka, H.J. Bauer, Experimental statistics
557 of droplet trajectory and air flow during aerodynamic fragmentation of liquid drops,
558 International Journal of Multiphase Flow, 47 (2012) 37-49.

559 [23] J. Han, G. Tryggvason, Secondary breakup of axisymmetric liquid drops. II. Impulsive
560 acceleration, Physics of Fluids, 13 (2001) 1554-1565.

561 [24] C. Aalburg, Deformation and breakup of round drop and nonturbulent liquid jets in
562 uniform crossflows, in: Aerospace Engineering and Scientic Computing, University of
563 Michigan, 2002.

564 [25] S. Khosla, C.E. Smith, Detailed Understanding of Drop Atomization by Gas Crossflow
565 Using the Volume of Fluid Method, in: ILASS Americas, Toronto, Canada, 2006.

566 [26] S. Quan, D.P. Schmidt, Direct numerical study of a liquid droplet impulsively
567 accelerated by gaseous flow, Physics of Fluids, 18 (2006) 103103.

568 [27] A.R. Wadhwa, V. Magi, J. Abraham, Transient deformation and drag of decelerating
569 drops in axisymmetric flows, Physics of Fluids, 19 (2007) 113301.

570 [28] F. Xiao, M. Dianat, J.J. McGuirk, LES of Single Droplet and Liquid Jet Primary Break-
571 up Using a Coupled Level Set/Volume of Fluid Method, in: 12th ICLASS, Heidelberg,
572 Germany, 2012.

573   [29] P. Khare, V. Yang, Drag Coefficients of Deforming and Fragmenting Liquid Droplets,

574   in: ILASS Americas, 2013.

575   [30] M. Jalaal, K. Mehravaran, Transient growth of droplet instabilities in a stream, Physics

576   of Fluids, 26 (2014) 012101.

577   [31] M. Jain, R.S. Prakash, G. Tomar, R.V. Ravikrishna, Secondary breakup of a drop at

578   moderate Weber numbers, Proceedings of the Royal Society of London A: Mathematical,

579   Physical and Engineering Sciences, 471 (2015).

580   [32] W. Yang, M. Jia, K. Sun, T. Wang, Influence of density ratio on the secondary

581   atomization of liquid droplets under highly unstable conditions, Fuel, 174 (2016) 25-35.

582   [33] G. Strotos, I. Malgarinos, N. Nikolopoulos, M. Gavaises, Predicting droplet deformation

583   and breakup for moderate Weber numbers, International Journal of Multiphase Flow, 85

584   (2016) 96–109.

585   [34] S.D. Givler, J. Abraham, Supercritical droplet vaporization and combustion studies,

586   Progress in Energy and Combustion Science, 22 (1996) 1-28.

587   [35] J. Bellan, Supercritical (and subcritical) fluid behavior and modeling: drops, streams,

588   shear and mixing layers, jets and sprays, Progress in Energy and Combustion Science, 26

589   (2000) 329-366.

590   [36] S.S. Sazhin, Advanced models of fuel droplet heating and evaporation, Progress in

591   Energy and Combustion Science, 32 (2006) 162-214.

592   [37] H.Y. Erbil, Evaporation of pure liquid sessile and spherical suspended drops: A review,

593   Advances in Colloid and Interface Science, 170 (2012) 67-86.

594   [38] M. Renksizbulut, R.J. Haywood, Transient droplet evaporation with variable properties

595   and internal circulation at intermediate Reynolds numbers, International Journal of

596   Multiphase Flow, 14 (1988) 189-202.

597   [39] R.J. Haywood, R. Nafziger, M. Renksizbulut, Detailed examination of gas and liquid

598   phase transient processes in convective droplet evaporation, Journal of Heat Transfer, 111

599   (1989) 495-502.

600 [40] C.H. Chiang, M.S. Raju, W.A. Sirignano, Numerical analysis of convecting, vaporizing
601 fuel droplet with variable properties, International Journal of Heat and Mass Transfer, 35
602 (1992) 1307-1324.

603 [41] C.M. Megaridis, Comparison between experimental measurements and numerical
604 predictions of internal temperature distributions of a droplet vaporizing under high-
605 temperature convective conditions, Combustion and Flame, 93 (1993) 287-302.

606 [42] A.T. Shih, C.M. Megaridis, Suspended droplet evaporation modeling in a laminar
607 convective environment, Combustion and Flame, 102 (1995) 256-270.

608 [43] A.T. Shih, C.M. Megaridis, Thermocapillary flow effects on convective droplet
609 evaporation, International Journal of Heat and Mass Transfer, 39 (1996) 247-257.

610 [44] M.M. Abou Al-Sood, M. Birouk, A numerical study of the effect of turbulence on mass
611 transfer from a single fuel droplet evaporating in a hot convective flow, International Journal
612 of Thermal Sciences, 46 (2007) 779-789.

613 [45] S. Raghuram, V. Raghavan, D.N. Pope, G. Gogos, Two-phase modeling of evaporation
614 characteristics of blended methanol–ethanol droplets, International Journal of Multiphase
615 Flow, 52 (2013) 46-59.

616 [46] J. Schlottke, B. Weigand, Direct numerical simulation of evaporating droplets, Journal of
617 Computational Physics, 227 (2008) 5215-5237.

618 [47] N. Ghata, B.D. Shaw, Computational modeling of the effects of support fibers on
619 evaporation of fiber-supported droplets in reduced gravity, International Journal of Heat and
620 Mass Transfer, 77 (2014) 22-36.

621 [48] C.M. Megaridis, W.A. Sirignano, Numerical modeling of a vaporizing multicomponent
622 droplet, Symposium (International) on Combustion, 23 (1990) 1413-1421.

623 [49] C.M. Megaridis, W.A. Sirignano, Multicomponent droplet vaporization in a laminar
624 convective environment, Combustion science and technology, 87 (1992) 27-44.

625 [50] C.M. Megaridis, Liquid-Phase Variable Property Effects in Multicomponent Droplet
626 Convective Evaporation, Combustion Science and Technology, 92 (1993) 291 - 311.

627 [51] M. Renksizbulut, M. Bussmann, Multicomponent droplet evaporation at intermediate

628 Reynolds numbers, International Journal of Heat and Mass Transfer, 36 (1993) 2827-2835.

629 [52] G. Strotos, M. Gavaises, A. Theodorakakos, G. Bergeles, Numerical investigation of the

630 evaporation of two-component droplets, Fuel, 90 (2011) 1492-1507.

631 [53] R. Banerjee, Numerical investigation of evaporation of a single ethanol/iso-octane

632 droplet, Fuel, 107 (2013) 724-739.

633 [54] G. Strotos, I. Malgarinos, N. Nikolopoulos, M. Gavaises, Predicting the evaporation rate

634 of stationary droplets with the VOF methodology for a wide range of ambient temperature

635 conditions, International Journal of Thermal Sciences, 109 (2016) 253–262.

636 [55] R.J. Haywood, M. Renksizbulut, G.D. Raithby, Numerical solution of deforming

637 evaporating droplets at intermediate Reynolds numbers, Numerical Heat Transfer; Part A:

638 Applications, 26 (1994) 253-272.

639 [56] R.J. Haywood, M. Renksizbulut, G.D. Raithby, Transient deformation and evaporation

640 of droplets at intermediate Reynolds numbers, International Journal of Heat and Mass

641 Transfer, 37 (1994) 1401-1409.

642 [57] Z.S. Mao, T. Li, J. Chen, Numerical simulation of steady and transient mass transfer to a

643 single drop dominated by external resistance, International Journal of Heat and Mass

644 Transfer, 44 (2001) 1235-1247.

645 [58] M. Hase, B. Weigand, Transient heat transfer of deforming droplets at high Reynolds

646 numbers, International Journal of Numerical Methods for Heat & Fluid Flow, 14 (2003) 85 -

647 97.

648 [59] J. Schlottke, E. Dulger, B. Weigand, A VOF-based 3D numerical investigation of

649 evaporating, deformed droplets, Progress in Computational Fluid Dynamics, an International

650 Journal, 9 (2009) 426-435.

651 [60] R.F.L. Cerqueira, E.E. Paladino, C.R. Maliska, A computational study of the interfacial

652 heat or mass transfer in spherical and deformed fluid particles flowing at moderate Re

653 numbers, Chemical Engineering Science, 138 (2015) 741-759.

654 [61] G. Strotos, I. Malgarinos, N. Nikolopoulos, M. Gavaises, Numerical investigation of
655 aerodynamic droplet breakup in a high temperature gas environment, Fuel, 181 (2016) 450-
656 462.

657 [62] A. Theodorakakos, G. Bergeles, Simulation of sharp gas–liquid interface using VOF
658 method and adaptive grid local refinement around the interface, International Journal for
659 Numerical Methods in Fluids, 45 (2004) 421-439.

660 [63] I. Malgarinos, N. Nikolopoulos, M. Marengo, C. Antonini, M. Gavaises, VOF
661 simulations of the contact angle dynamics during the drop spreading: Standard models and a
662 new wetting force model, Advances in Colloid and Interface Science, 212 (2014) 1-20.

663 [64] R.H. Perry, D.W. Green, Perry's Chemical Engineers' Handbook, 7th ed., McGraw-Hill,
664 1997.

665 [65] B.E. Poling, J.M. Prausnitz, J.P. O'Connell, Properties of Gases and Liquids (5th
666 Edition), in, McGraw-Hill, 2001.

667 [66] ANSYS®FLUENT, Release 14.5, Theory Guide, in, 2012.

668 [67] I. Malgarinos, N. Nikolopoulos, M. Gavaises, Coupling a local adaptive grid refinement
669 technique with an interface sharpening scheme for the simulation of two-phase flow and free-
670 surface flows using VOF methodology, Journal of Computational Physics, 300 (2015) 732-
671 753.

672 [68] G. Strotos, I. Malgarinos, N. Nikolopoulos, K. Papadopoulos, A. Theodorakakos, M.
673 Gavaises, Performance of VOF methodology in predicting the deformation and breakup of
674 impulsively accelerated droplets in: 13th ICLASS, Tainan, Taiwan, 2015.

675 [69] R. Clift, J.R. Grace, M.E. Weber, Bubbles, drops and particles, Academic Press, New
676 York, 1978.

677 [70] E.E. Michaelides, Particles, bubbles & drops: their motion, heat and mass transfer, World
678 Scientific, 2006.

679 [71] F.P. Incropera, D.P. de Witt, Fundamentals of Heat and Mass Transfer 3rd ed., Wiley,
680 New York, 1990.

681   [72] M. Seki, H. Kawamura, K. Sanokawa, Transient temperature profile of a hot wall due to
682   an impinging liquid droplet, Journal of Heat Transfer, 100 (1978) 167-169.

683   [73] G. Strotos, G. Aleksis, M. Gavaises, K.-S. Nikas, N. Nikolopoulos, A. Theodorakakos,
684   Non-dimensionalisation parameters for predicting the cooling effectiveness of droplets
685   impinging on moderate temperature solid surfaces, International Journal of Thermal Sciences,
686   50 (2011) 698-711.

687   [74] G. Strotos, N. Nikolopoulos, K.-S. Nikas, K. Moustris, Cooling effectiveness of droplets
688   at low Weber numbers: Effect of temperature, International Journal of Thermal Sciences, 72
689   (2013) 60-72.

690   [75] M. Renksizbulut, M. Bussmann, X. Li, Droplet vaporization model for spray
691   calculations, Particle & Particle Systems Characterization, 9 (1992) 59-65.

692   [76] B. Lafaurie, C. Nardone, R. Scardovelli, S. Zaleski, G. Zanetti, Modelling Merging and
693   Fragmentation in Multiphase Flows with SURFER, Journal of Computational Physics, 113
694   (1994) 134-147.

695

696